Understanding the unique Ohmic-junction for enhancing the photocatalytic activity of CoS$_2$/MgIn$_2$S$_4$ towards hydrogen production

Jiangshan Li [a,1], Jun Yao [a,1], Qiang Yu [a], Xiao Zhang [a], Sónia A.C. Carabineiro [b], Xianqiang Xiong [a,*], Chenglin Wu [a], Kangle Lv [c,*]

[a] School of Pharmaceutical and Chemical Engineering, Taizhou University, Jiaojiang 318000, China
[b] LAQV-REQUIMTE, Department of Chemistry, NOVA School of Science and Technology, Universidade NOVA de Lisboa, Caparica 2829-516, Portugal
[c] College of Resources and Environment, South-Central Minzu University, Wuhan 430074, China

ARTICLE INFO

ABSTRACT

MgIn$_2$S$_4$ is a photocatalyst with a suitable band gap for renewable energy production, but its effectiveness is hindered by pronounced photocorrosion, insufficient surface active sites and rapid charge recombination. Herein, we report the synthesis of CoS$_2$/MgIn$_2$S$_4$ Ohmic junction with a robust internal electric field. The optimized CoS$_2$/MgIn$_2$S$_4$ photocatalyst with a CoS$_2$ loading of 20.5 wt%, depicts a maximum H$_2$ evolution rate of 290 μmol g^{-1} h^{-1}, which is 3.1 times higher than the value of MgIn$_2$S$_4$. The improved photocatalytic activity of CoS$_2$/MgIn$_2$S$_4$ can be attributed to the intimate Ohmic junction at the CoS$_2$/MgIn$_2$S$_4$ interface, which promotes effective photoelectron transfer from MgIn$_2$S$_4$ to CoS$_2$. Simultaneously, CoS$_2$ can act as an efficient surface cocatalyst, with an optimal hydrogen-adsorption Gibbs free energy, enabling highly efficient proton reduction at the catalyst/H$_2$O interface. The present work introduces a novel approach to modulate interfaces, creating transition metal sulfide cocatalysts for photocatalysts, resulting in high photocatalytic performance.

1. Introduction

In light of the pressing challenges dealing with environmental pollution and energy crisis, the need to develop sustainable and clean energy solutions to address the imminent fuel issue becomes increasingly evident [1,2]. The process of photocatalytic hydrogen evolution, where abundant solar energy is harvested and converted into hydrogen energy, is considered a promising technology that can serve as a reliable source of clean energy for human society [3,4]. While numerous semiconductor-based photocatalysts have been optimized for H$_2$ production, photocatalytic technology still faces several obstacles, including narrow spectral response ranges, low carrier separation efficiency and insufficient redox-active sites [5–8]. 2D layered semiconductors are ideal photocatalysts, mainly due to their large specific area and excellent electron mobility [9–11]. Moreover, these materials offer a larger number of active sites, with abundant channels for the migration and separation of photogenerated charge carriers. This is highly advantageous for enhancing the photocatalytic H$_2$ evolution [12, 13].

MgIn$_2$S$_4$ stands out as a unique material, with distinct properties and advantages for photocatalysis [14]. These include an optimal band gap for effective visible light absorption, robust chemical and thermal stability, ensuring durability and consistent performance, and a composition of abundant, non-toxic and cost-effective elements [15,16]. Due to these advantages, MgIn$_2$S$_4$ exhibits a wide range of applications in photocatalysis, including environmental pollution degradation [16], CO$_2$ reduction [17], photoreduction of heavy metal ions [18], H$_2$ evolution [15] and hydrocarbon evolution [19]. However, pristine MgIn$_2$S$_4$ shows some drawbacks, including weak separation efficiency of photoexcitons, photocorrosion and poor cycle stability, which adversely affect its photocatalytic performance [20]. Several approaches have been proposed in order to overcome these flaws, including doping [20], morphological regulation [21] and construction of heterojunctions [15]. Most modification research primarily concentrates on the treatment of environmental pollutants, while the investigations toward H$_2$ evolution are still limited. A detailed examination of the existing literature reveals that only six studies report the performance of MgIn$_2$S$_4$-based materials in terms of solar H$_2$ production. Moreover, these works primarily focus

---

* Corresponding authors.
   E-mail addresses: 11337061@zju.edu.cn (X. Xiong), lvkangle@mail.scuec.edu.cn (K. Lv).
   [1] These authors contributed equally to this work.

on the use of the heterojunction strategy to enhance the photocatalytic activity of $MgIn_2S_4$ through its coupling with other semiconductors. For example, Parida and colleagues have reported on two pn junctions (B-doped $C_3N_4/MgIn_2S_4$ [15] and p-MoS_2/n-$MgIn_2S_4$ [20]) and two Z-scheme heterojunctions ($MgIn_2S_4$/UiO-66-NH_2 [22] and $TiO_2@$-$Ti_3C_2/MgIn_2S_4$ [23]), effectively promoting charge separation and migration. This results in a remarkably enhanced rate of H_2 evolution. Additionally, Niu *et al.* have reported a type-II $MgIn_2S_4$/CdS heterojunction for photocatalytic H_2 evolution, demonstrating an enhanced H_2 production of 52.14 μmol g^{-1} h^{-1} [16]. Despite these successes, the obtained H_2 evolution rate is considerably lower than the amount achieved using other ternary metal sulfides, such as $ZnIn_2S_4$ [24] and $CdIn_2S_4$ [25]. Therefore, there is a compelling need for the research community to improve the photocatalytic performance of $MgIn_2S_4$ photocatalysts for H_2 production.

In many semiconductor photocatalysts, the loading of cocatalysts is an efficient method for enhancing photocatalytic performance [26–29]. This is because cocatalyst loading can suppress recombination of charge carriers by trapping electrons of semiconductor photocatalysts and provide active sites for surface proton reduction [27,30]. Conversely, conventional semiconductor/semiconductor heterojunctions primarily improve charge separation while making a smaller contribution to the charge transfer process at the catalyst/H_2O interface. Taking these factors into account, it can be predicted that the $MgIn_2S_4$/co-catalyst system will exhibit superior photocatalytic H_2 evolution activity compared to the traditional semiconductor/semiconductor heterojunctions. However, cocatalyst coupling with $MgIn_2S_4$ for photocatalytic H_2 evolution has not yet been reported.

Transition metal sulfides, including Co_9S_8, MoS_2, CoS_2, NiS and $NiCo_2S_4$ are extensively utilized as noble-metal free cocatalysts in semiconductor photocatalysts due to their satisfactory electrical conductivity and lower conduction band potentials [31–35]. These cocatalysts can effectively extract photogenerated electrons from semiconductor photocatalysts, promoting efficient charge separation and thereby enhancing the overall photocatalytic activity. Among the various transition metal sulfides, pyrite-type CoS_2 exhibits significant potential for cocatalyst utilization due to its exclusive metallic characteristics, extensive spectral absorption with 0 band gap, exceptional electrocatalytic hydrogen evolution reaction (HER) activity and excellent chemical stability [36]. The majority of other transition metal sulfides, however, exhibit semiconductor properties, characterized by limited electronic conductivity, thereby resulting in a limited improvement in hydrogen evolution performance [37]. In contrast, several studies demonstrate that CoS_2 enhances the photocatalytic H_2 evolution of CdS [36], C_3N_4 [38], and $ZnIn_2S_4$ [39] photocatalysts. Therefore, CoS_2 has the potential to act as a promising cocatalyst for increasing the hydrogen evolution capabilities of the $MgIn_2S_4$ photocatalyst. First, considering the band structure, CoS_2 exhibits metallic properties and a lower work function range of 4.7–5.1 eV [40], making it possible to form an Ohmic junction- with $MgIn_2S_4$. This prevents reverse carrier transport, thereby improving carrier separation and migration efficiency. Moreover, considering interface quality, the cubic crystalline structure of CoS_2 closely aligns with that of cubic $MgIn_2S_4$, leading to a favorable lattice match at the interface between the two phases. Specifically, the coordinatively unsaturated sulfur atoms found on the surface of $MgIn_2S_4$ can function as anchoring sites for cobalt atoms from CoS_2, leading to the formation of interfacial cobalt-sulfur bonds. These interfacial bonds are similar to the bulk cobalt-sulfur bond present in CoS_2, potentially acting as an atomic-level interfacial bridge that facilitates electron transfer. Given these advantages, CoS_2 and $MgIn_2S_4$ can be coupled to create Ohmic junctions with efficient electron transfer channels at the $CoS_2/MgIn_2S_4$ interface. Simultaneously, CoS_2 can also promote electron injection at the catalyst/H_2O interface, due to its catalytic effect, leading to an overall improvement in the photocatalytic H_2 evolution activity. Despite these potential benefits, there is currently no publication dealing with the construction of a similar design, and the precise

contribution of CoS_2 in enhancing the activity of photocatalytic hydrogen evolution remains insufficiently elucidated, thus needing investigation.

This study introduces a series of $CoS_2/MgIn_2S_4$ heterojunction photocatalysts, synthesized through a facile two-step hydrothermal method that combines CoS_2 nanoparticles and 3D $MgIn_2S_4$ micro-flowers. The 3D micro-flower-like structure of $MgIn_2S_4$, characterized by a significant surface area, promotes the effective dispersion of CoS_2 nanoparticles. Under Xe-light illumination, the composite containing 20.5 wt% of CoS_2 nanoparticles exhibits a remarkable enhancement in the photocatalytic H_2 evolution, achieving a maximum rate 3.1 times higher than the value of pristine $MgIn_2S_4$ micro-flowers. The enhancement in activity surpasses that of the noble-metal-modified $MgIn_2S_4$ system, highlighting the particularly effective role of CoS_2 in enhancing the photocatalytic performance of $MgIn_2S_4$. Additionally, we demonstrate for the first time that CoS_2 can form a robust Ohmic junction with $MgIn_2S_4$ due to a matched band structure, facilitating the effective extraction of photogenerated electrons from $MgIn_2S_4$ to CoS_2 through an internal electric field (IEF). This discovery is novel, as almost all other reported CoS_2-modified semiconductor systems demonstrate a Schottky junction charge mechanism [5,40], instead of the Ohmic junction. The Ohmic junctions enhance the separation efficiency of photogenerated electron-hole pairs, compared to the Schottky junctions. This enhancement occurs by eliminating the interfacial energy barrier, leading to an increased availability of charge carriers for photocatalytic reactions. This insight is supported by Density Functional Theory (DFT) calculations, *in situ* irradiated X-ray photoelectron spectroscopy, and KPFM. Moreover, this work elucidates the catalytic role of CoS_2, demonstrating its capability to modify the surface proton reduction kinetics. This study also highlights the synergy between transition metal sulfide and semiconductor photocatalysts, demonstrating their potential for optimizing photocatalysis.

2. Experimental section

2.1. Synthesis of CoS_2

The CoS_2 compound was synthesized using a simple hydrothermal technique [41]. In detail, a solution was prepared by dissolving 4 mmol of $Na_2S_2O_3 \cdot 6 H_2O$ and 2 mmol of $Co(NO_3)_2 \cdot 6 H_2O$ in 40 mL of deionized water, which was then stirred for 10 min. Subsequently, 20 mL of ethylene glycol and 10 mL of ethanol were introduced into the solution, and the mixture was stirred for 2 h. The resulting CoS_2 particles were thoroughly washed with deionized water and ethanol, and subsequently dried at 60 °C for 12 h.

2.2. Synthesis of $CoS_2/MgIn_2S_4$

Scheme 1 provides a concise overview of the process used to synthesize the $CoS_2/MgIn_2S_4$ composite. In this method, CoS_2 nanoparticles were prepared through a hydrothermal method, as previously described. Subsequently, 0.5 mmol of $MgCl_2$ and 1 mmol of $InCl_3$ were dissolved in 70 mL of ethylene glycol using a supersonic apparatus for 30 min. The synthesized CoS_2 (in varying amounts) was combined with thioacetamide (4 mmol) in the above solution. The resulting aqueous solution was magnetically stirred for 30 min, transferred to a stainless autoclave and heated for 12 h at 180 °C. After natural cooling, the resultant precipitate was collected by centrifugation and washed thrice with deionized water and absolute ethanol. Finally, the resulting product was dried overnight at 60 °C. Synthesized samples were denoted as *x* wt% $CoS_2/MgIn_2S_4$, where *x* wt% represents the weight proportions of CoS_2 to $MgIn_2S_4$ in the composite materials, as determined by ICP-AES. The same synthetic procedure was used to produce bare $MgIn_2S_4$, except for the addition of CoS_2 nanoparticles.

Further details on characterization, photocatalytic hydrogen production and electrochemical measurements can be found in the
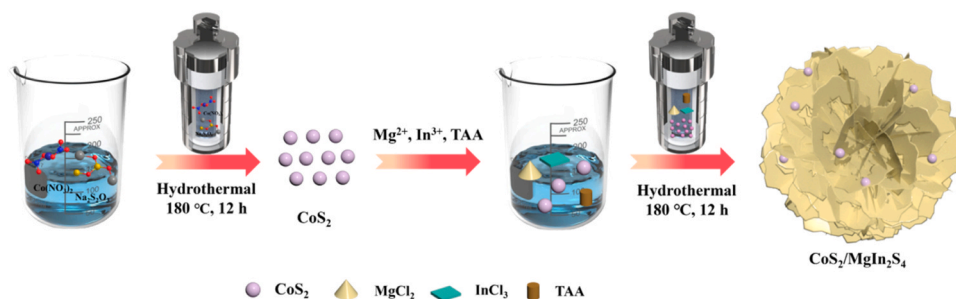
Scheme 1. Illustration of the preparation process of $CoS_2/MgIn_2S_4$.

Supporting Information.

3. Results and discussion

3.1. Characterization of photocatalysts

The present study demonstrates the successful synthesis of a series of robustly coupled $CoS_2/MgIn_2S_4$ heterojunction photocatalysts through a straightforward two-step hydrothermal method, as illustrated in Scheme 1. In the initial hydrothermal treatment, CoS_2 crystal nuclei are generated through the nucleation of cobalt nitrate and sodium thiosulfate precursors. Subsequently, these nuclei undergo a growth process, leading to the aggregation of some CoS_2 nanoparticles, due to reduced surface energy. Under high temperature and pressure conditions, the initial crystal nucleus of $MgIn_2S_4$ tend to immobilize on the CoS_2 surface over time, driven by surface energies, and eventually self-assemble *in situ* to form a marigold flower-like sphere structure of $MgIn_2S_4$, resulting in heterogeneous $CoS_2/MgIn_2S_4$ nanocomposites.

Fig. 1a-c show SEM images highlighting the morphological characteristics of CoS_2, $MgIn_2S_4$ and 20.5 wt% $CoS_2/MgIn_2S_4$ composites. $MgIn_2S_4$ shows a micrometer-sized architecture composed of numerous nanoflakes interconnected by numerous nanosheets (Fig. 1a) These nanoflake sheets form several microspheres that resemble marigold micro-flowers, with diameters ranging from 1.5 to 3.0 μm. Fig. 1b presents a SEM image of CoS_2 along with the corresponding particle size distribution histogram in the inset. The predominant particle sizes range from 0.3 μm to 1.0 μm, with the maximum observed size reaching 1.33 μm. In contrast to pure $MgIn_2S_4$, the 20.5 wt% $CoS_2/MgIn_2S_4$ composite (Fig. 1c) displays well-dispersed CoS_2 nanoparticles loaded on the nanosheets, indicating the successful coupling of CoS_2 to the flower-like $MgIn_2S_4$.

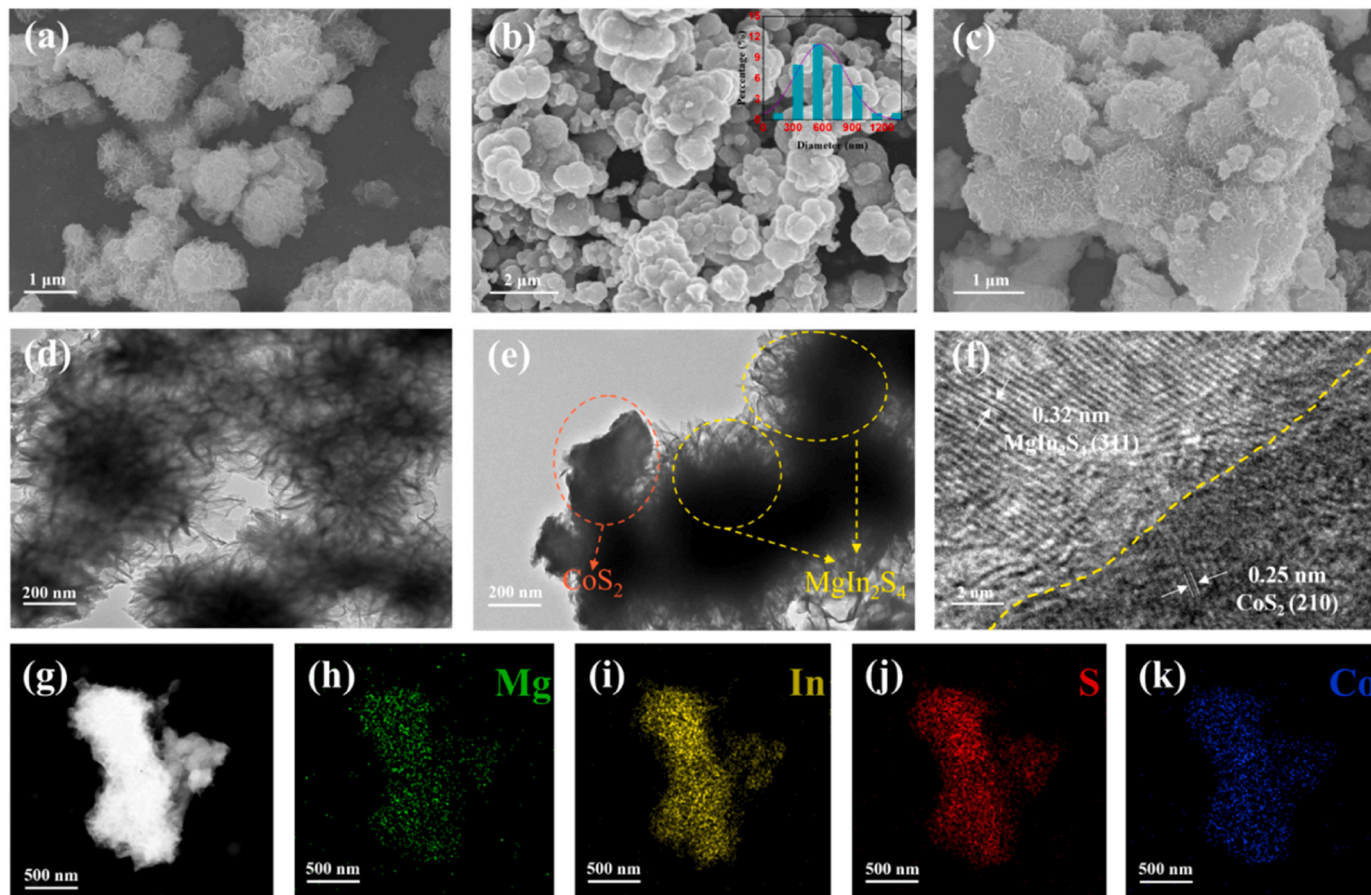Transmission electron microscopy (TEM) and colour elemental

Fig. 1. (a-c) SEM images of $MgIn_2S_4$, CoS_2 and 20.5 wt% $CoS_2/MgIn_2S_4$. (d-e) TEM images of $MgIn_2S_4$ and 20.5 wt% $CoS_2/MgIn_2S_4$. (f) HRTEM and (g-k) elemental mapping images of 20.5 wt% $CoS_2/MgIn_2S_4$.

mapping analyses can be employed to provide a comprehensive characterization of the microstructure of $MgIn_2S_4$ and 20.5 wt% $CoS_2/MgIn_2S_4$ (Fig. 1). In the TEM image of pristine $MgIn_2S_4$ (Fig. 1d), a distinct 3D marigold flower-like structure is clearly visible, formed by interlacing flake-type $MgIn_2S_4$ nanosheets. $MgIn_2S_4$ displays lattice fringes of approximately 0.32 nm, corresponding to its (311) plane (Fig. S1). In contrast, Fig. 1e-f reveal a distinct heterojunction pattern of the $CoS_2/MgIn_2S_4$ composite. The CoS_2 nanoparticles are distributed on the surface of $MgIn_2S_4$ micro-flowers, closely interconnecting with each other in such a way that the gauze-like edge of $MgIn_2S_4$ contacts with CoS_2 nanoparticles, demonstrating the fabrication of heterojunction photocatalysts. In a highly magnified HRTEM image (Fig. 1f), two different lattice spacings are observed, separated by an intimate junction between the two photocatalysts, namely 0.25 nm, corresponding to the cubic CoS_2 plane (210), and 0.32 nm, that corresponds to the cubic $MgIn_2S_4$ plane (311). Moreover, the colour elemental mapping images depicted in Fig. 1h-k illustrate the coexistence and uniform dispersion of multiple elements within the 20.5 wt% $CoS_2/MgIn_2S_4$ heterojunction photocatalysts.

X-ray diffraction measurements can be used to identify the crystal structures and phases of $MgIn_2S_4$, CoS_2 and $CoS_2/MgIn_2S_4$ composites with varying CoS_2 contents (Fig. 2a). In the case of pristine $MgIn_2S_4$, the three characteristic diffraction peaks at 27.8°, 33.7° and 48.4° can be assigned to (311), (400), and (440) planes of cubic $MgIn_2S_4$ (JCPDS #31–0792), respectively [14,18]. For pure CoS_2, the diffraction peaks at 2θ values of 27.8°, 32.3°, 36.2°, 39.8°, 46.4°, and 54.9° can be successfully indexed to the (111), (200), (210), (211), (220), and (311) planes of cubic CoS_2 (JCPDS #41–1471), respectively [40]. In both samples, no diffraction peaks attributed to impurities are observed, demonstrating the high purity of CoS_2 and $MgIn_2S_4$. In the $CoS_2/MgIn_2S_4$ composites, all X-ray diffraction (XRD) peaks display a combination of $MgIn_2S_4$ and CoS_2, with peak intensity increasing with CoS_2 content increase. This indicates the successful coupling of $MgIn_2S_4$ and

CoS_2.

N_2 adsorption-desorption can be used to assess the surface areas and pore sizes of pristine $MgIn_2S_4$ nanosheets, pure CoS_2 nanoparticles and 20.5 wt% $CoS_2/MgIn_2S_4$ composites. The N_2 adsorption-desorption isotherms for the three samples are presented in Fig. 2b. CoS_2 exhibits a type III isotherm, whereas $MgIn_2S_4$ displays a shape similar to a type IV isotherm with a distinctive H3-type hysteresis loop, indicating the presence of mesopores. The mesoporous structure is likely formed by the aggregation of 2D $MgIn_2S_4$ nanosheets, creating 3D micro-flowers [42]. The isotherm of the 20.5 wt% $CoS_2/MgIn_2S_4$ composite is similar to the isotherm obtained for pristine $MgIn_2S_4$, but with an increased adsorbed volume. The Barrett-Joyner-Halenda (BJH) method, utilizing the absorption branch of the isotherm, can be used to further confirm the presence of the mesoporous structure in these three samples. The BJH adsorption average pore diameters are approximately 14.43 nm for $MgIn_2S_4$ and 13.93 nm for the 20.5 wt% $CoS_2/MgIn_2S_4$, both falling within the mesoporous range. According to BET calculations, the surface areas of $MgIn_2S_4$, CoS_2 and the 20.5 wt% $CoS_2/MgIn_2S_4$ composite are 15.22, 4.08, and 28.26 m^2 g^{-1}, respectively (Table S1). Clearly, the $CoS_2/MgIn_2S_4$ composite exhibits a significant improvement in the BET surface area compared to pristine $MgIn_2S_4$. This increase can be attributed to the efficient dispersion of CoS_2 nanoparticles on $MgIn_2S_4$ nanosheets, as observed in the SEM images (Fig. 1), which effectively reduces the aggregation of CoS_2 particles by forming heterogeneous interfaces. The good dispersion of CoS_2 can be attributed to the positive role of the high surface energy of $MgIn_2S_4$ nanosheets during the *in situ* growth process, acting as an efficient platform for the distribution of CoS_2 nanoparticles. To validate whether the dispersion of CoS_2 is indeed responsible for the enhanced specific surface area, we conducted a comparative study involving the direct physical mixing of CoS_2 aggregates with $MgIn_2S_4$ nanosheets through grinding, followed by a comparison of their specific surface areas (Fig. S2). SEM analysis (Fig. S3) revealed significant aggregation of CoS_2 within the physically mixed
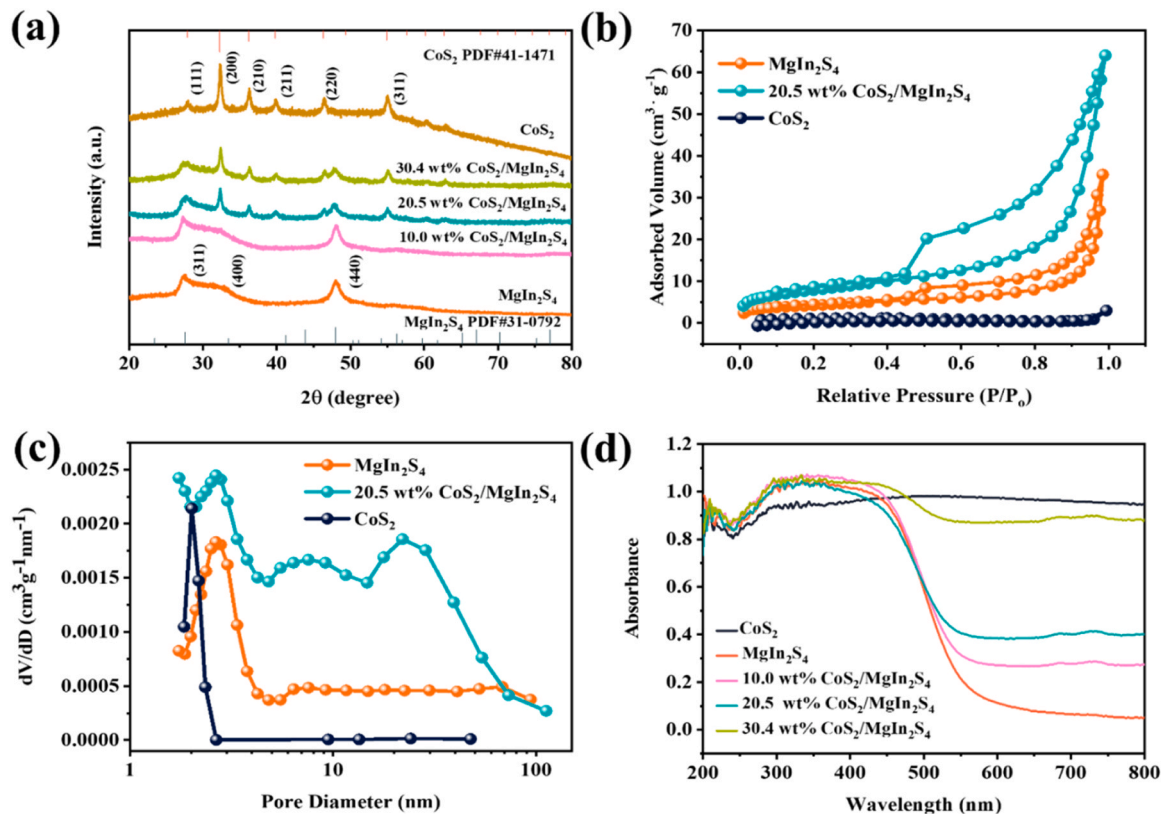

Fig. 2. (a) XRD diffractograms of CoS_2, $MgIn_2S_4$, and *x* wt% $CoS_2/MgIn_2S_4$. (b) N_2 adsorption-desorption isotherms and (c) pore size distribution curves of $MgIn_2S_4$, CoS_2 and 20.5 wt% $CoS_2/MgIn_2S_4$. d) UV–vis spectra of CoS_2, $MgIn_2S_4$ and *x* wt% $CoS_2/MgIn_2S_4$.

$CoS_2/MgIn_2S_4$ composite. As expected, the specific surface area of this mixture (13.56 m^2 g^{-1}) was markedly lower, compared to that of the $CoS_2/MgIn_2S_4$ (28.26 m^2 g^{-1}) synthesized through a two-step hydrothermal approach. This demonstrates the substantial impact of CoS_2 dispersion on the improvement of the specific surface area.

In this study, the optical properties of $MgIn_2S_4$ nanosheets, pure CoS_2 nanoparticles and their composites have been investigated using ultraviolet-visible diffuse reflectance (UV–vis DRS) spectra (Fig. 2d). Pristine $MgIn_2S_4$ exhibits light absorption from the ultraviolet to the visible light region, with the absorption threshold at ~600 nm due to a direct optical transition [18]. The band gap value of $MgIn_2S_4$ is estimated to be approximately 2.18 eV using the Tauc plot (Fig. S4). In contrast to the bare $MgIn_2S_4$ samples, black CoS_2 exhibits broad absorption over the entire wavelength range of 200–800 nm. The $CoS_2/MgIn_2S_4$ hybrid photocatalysts display an obvious red shift in absorbance edge, compared to pure $MgIn_2S_4$. With increasing CoS_2 content, $CoS_2/MgIn_2S_4$ hybrid samples exhibit improved visible light absorption abilities. The enhanced light absorption is attributed to the background adsorption of black-colored CoS_2, confirming the successful loading of CoS_2 onto $MgIn_2S_4$.

3.2. Photocatalytic activity evaluation

The photocatalytic H_2 evolution on pure CoS_2, $MgIn_2S_4$,and $CoS_2/MgIn_2S_4$ composite photocatalysts has been evaluated under Xe lamp irradiation using a 20% TEOA (triethanolamine) aqueous solution as a sacrificial agent. The time curves of hydrogen evolution for pure CoS_2, $MgIn_2S_4$, and x wt% $CoS_2/MgIn_2S_4$ composite photocatalysts are presented in Fig. 3a. At 4 h of photoirradiation, the bare $MgIn_2S_4$ sample only exhibits a modest hydrogen evolution of 280 μmol g^{-1}. This result indicates the significantly low photocatalytic H_2 evolution activity of $MgIn_2S_4$ photocatalyst, likely attributed to its low charge separation and transfer efficiency. In addition, the neat CoS_2 shows no hydrogen evolution, aligning with previous findings [36,43,44]. Compared to
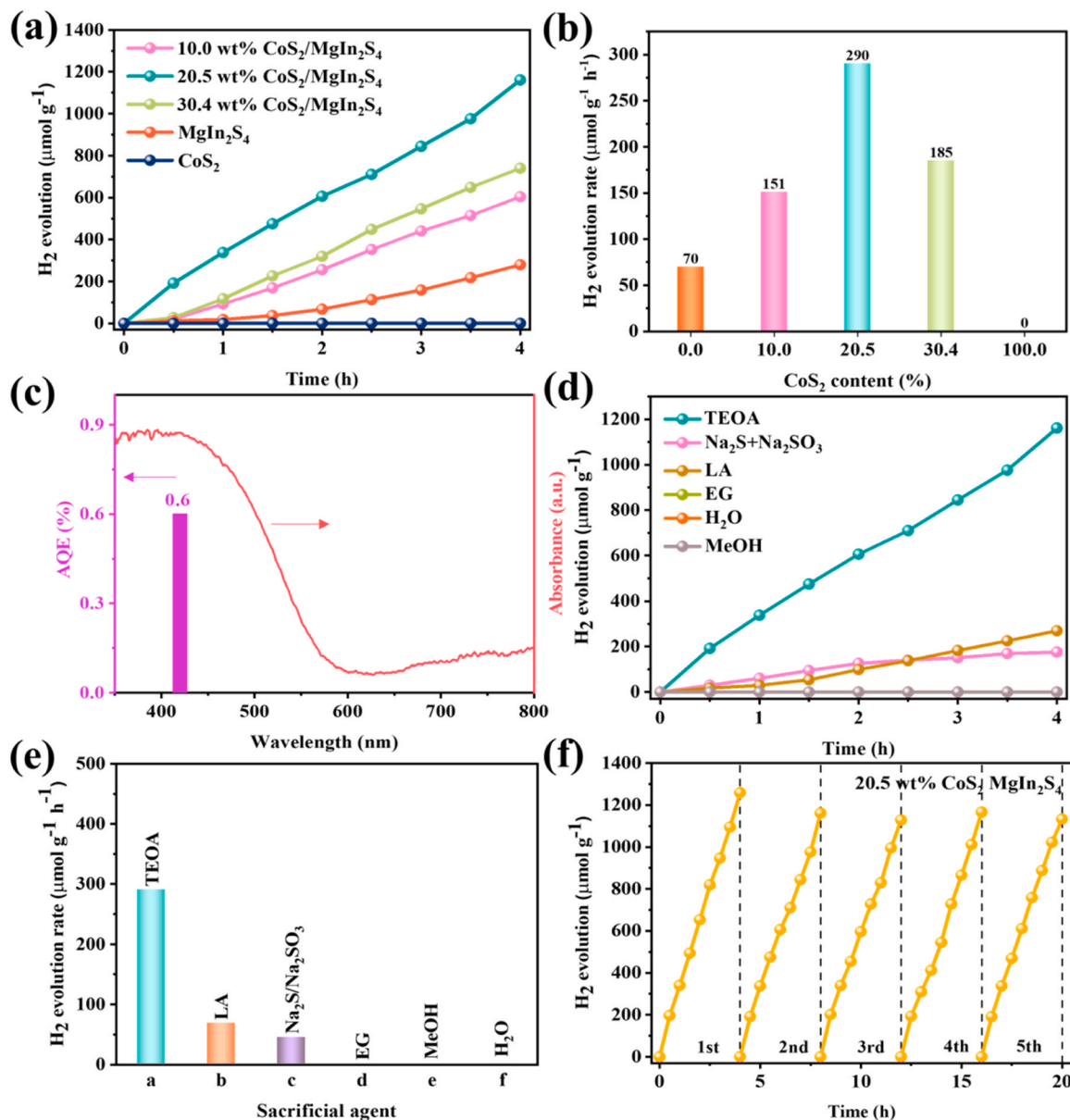

Fig. 3. (a) Time profiles of photocatalytic hydrogen generation of $MgIn_2S_4$, CoS_2, and x wt% $CoS_2/MgIn_2S_4$. (b) Rate of H_2 production on x wt% $CoS_2/MgIn_2S_4$. (c) Wavelength dependence of AQE for 20.5 wt% $CoS_2/MgIn_2S_4$ at 420 nm wavelength. (d) Time profiles of photocatalytic hydrogen generation and (e) photocatalytic hydrogen generation rate of the calculated H_2 evolution with various sacrificial agents for 20.5 wt% $CoS_2/MgIn_2S_4$. f) Cyclic H_2 evolution over 20.5 wt% $CoS_2/MgIn_2S_4$.

individual $MgIn_2S_4$ and CoS_2 photocatalysts, the $CoS_2/MgIn_2S_4$ composite photocatalysts demonstrate a significantly higher hydrogen evolution rate. As the CoS_2 content increases, the H_2 evolution of the composite photocatalysts also increases, reaching a maximum at 20.5 wt %, after which it declines. The decrease in the hydrogen evolution rate at higher CoS_2 loading (30.4 wt%) might be attributed to the light shielding effect of CoS_2, diminishing the light absorption of the $MgIn_2S_4$ photocatalyst and thereby reducing the generation of electron-hole pairs for the photocatalytic reaction.

The optimized 20.5 wt% $CoS_2/MgIn_2S_4$ photocatalyst exhibits an impressive H_2 evolution rate of 1160 µmol g^{-1} within 4 h of light irradiation, nearly 3.1 times higher than the value of the $MgIn_2S_4$ sample. At a wavelength of 420 nm, the 20.5 wt% $CoS_2/MgIn_2S_4$ photocatalyst demonstrates an apparent quantum efficiency (AQE) of 0.6% (Fig. 3c). It is noteworthy that, despite the relatively lower hydrogen production activity of the $CoS_2/MgIn_2S_4$ composite, compared to other ternary metal sulfides such as $ZnIn_2S_4$ [25,45], this discrepancy is likely attributable to the intrinsic defects within $MgIn_2S_4$, limiting carrier mobility towards the surface. Nevertheless, the 20.5 wt% $CoS_2/MgIn_2S_4$ photocatalyst developed in this study demonstrates similar or even superior performance compared to other $MgIn_2S_4$-based photocatalysts. For example, Jing et al. have examined the activity of a PANI-$MgIn_2S_4$ composite for photocatalytic H_2 production and have reported a rate of 17.53 µmol g^{-1} h^{-1}, significantly lower than the rate observed in our system [18]. Similarly, Liu et al. have obtained a 3D/1D $MgIn_2S_4$/CdS heterojunction system, with a H_2 generation rate of only 52.14 µmol g^{-1} h^{-1} in TEOA aqueous solution [16]. Furthermore, we have conducted a comparative analysis of the photocatalytic H_2 activity between the 20.5 wt% $CoS_2/MgIn_2S_4$ system and noble-metal (Au or Pt) modified $MgIn_2S_4$ systems, under identical experimental conditions. Our findings reveal that the introduction of Au results in a 2-fold increase in H_2 production on $MgIn_2S_4$ (Fig. S5), while the presence of Pt enhances the activity by only 31%, both being lower than the enhancement achieved with 20.5 wt% $CoS_2/MgIn_2S_4$. These results unequivocally demonstrate the significant improvement of the photocatalytic activity of $MgIn_2S_4$ through the introduction of the CoS_2 cocatalyst.

A systematic study of the impact of various sacrificial reagents, namely lactic acid (LA), Na_2S/Na_2SO_3, methanol (MeOH), and ethylene glycol (EG) on the hydrogen production activity of 20.5 wt% $CoS_2/MgIn_2S_4$ photocatalysts is presented in Fig. 3d. The results indicate a significant decrease in hydrogen production activity when these scavengers are employed, with LA exhibiting the highest hydrogen production activity at only 67 µmol g^{-1} h^{-1}. In this study, TEOA stands out as the most effective among the tested scavengers, possibly due to its alkaline nature, which enhances its absorption capability [46]. This increases the surface electronegativity of the catalyst, facilitating the capture of positively charged holes and resulting in optimal hydrogen production activity.

In addition, the H_2 yield of the optimized catalyst (20.5 wt% $CoS_2/MgIn_2S_4$) has been evaluated in TEOA aqueous solution under Xe light irradiation for 20 h, as illustrated in Fig. 3f. After five cycles of experimentation, the 20.5 wt% $CoS_2/MgIn_2S_4$ material has demonstrated excellent recyclability, retaining 97.5% of its original activity. The structural stability of 20.5 wt% $CoS_2/MgIn_2S_4$ has been further evaluated through XRD, scanning electron microscopy (SEM), and XPS spectra (Figs. S6–8). Post-cycle measurements reveal that the crystal structure and morphology of the 20.5 wt% $CoS_2/MgIn_2S_4$ hybrid remain virtually unchanged, and the XPS intensity is almost unaltered except for a slight shift in binding energy, confirming its remarkable stability.

3.3. Photocatalytic mechanism study

In photocatalytic processes, multiple factors contribute to the overall photocatalytic activity, including phase crystallinity, microstructure, specific area, light absorption, charge separation and transfer. The synergy of these key factors collectively determines the overall

photocatalytic efficiency. Given that $CoS_2/MgIn_2S_4$ hybrid photocatalysts exhibit similar crystallinity and microstructure, the enhanced photocatalytic activity cannot be solely attributed to alterations in these variables. As depicted in Fig. 2d, the CoS_2 decorated $MgIn_2S_4$ demonstrates a broader photo-absorption range at 550–800 nm, compared to bare $MgIn_2S_4$, suggesting a potential contribution to increased photoactivity. However, the control experiment in Fig. S9 reveals that the $CoS_2/MgIn_2S_4$ photocatalyst fails to produce H_2 when irradiated with light at wavelengths $\geq$ 550 nm. This result indicates that the increased photo-absorption is not the sole factor enhancing the photocatalytic activity. Therefore, the improved photocatalytic activity is primarily attributed to faster charge separation and/or more efficient charge injection facilitated by the tight Ohmic-Junction interactions between CoS_2 and $MgIn_2S_4$. Notably, the H_2 evolution rate is significantly lower when CoS_2 and $MgIn_2S_4$ are physically mixed, compared to the hydrothermally produced 20.5 wt% $CoS_2/MgIn_2S_4$ composite presented in this study (Fig. S10). This observation provides evidence that the formation of an intimate $CoS_2/MgIn_2S_4$ heterojunction is crucial for achieving high-efficiency H_2 evolution.

In the following sections, the impact of tight $CoS_2/MgIn_2S_4$ heterojunctions on carrier separation and transfer dynamics is explored. The photoluminescence (PL) spectrum has been employed to investigate the high separation efficiency between photogenerated holes and electrons in $CoS_2/MgIn_2S_4$ hybrid photocatalysts. The steady-state fluorescence spectra of $MgIn_2S_4$ and 20.5 wt% $CoS_2/MgIn_2S_4$ composites with excitation wavelengths of 300 nm are presented in Fig. 4a. Bare $MgIn_2S_4$ displays an intense and broad spectrum of fluorescence emission between 400 and 700 nm, indicative of charge carrier recombination and energy relaxation [18]. The PL intensity of $MgIn_2S_4$ significantly decreases with the incorporation of CoS_2, suggesting that $CoS_2/MgIn_2S_4$ provides better photoinduced electron-hole separation than $MgIn_2S_4$. Time-resolved transient photoluminescence spectra have also been used to further explore the charge separation process on both pristine $MgIn_2S_4$ and $CoS_2/MgIn_2S_4$ samples. Fig. 4b shows the fluorescence decay curves analysed using a bi-exponential model [47,48]. Remarkably, the 20.5 wt% $CoS_2/MgIn_2S_4$ sample exhibits a longer average decay lifetime (0.47 ns) compared to bare $MgIn_2S_4$ (0.42 ns), indicating an effective enhancement in charge separation within the $CoS_2/MgIn_2S_4$ heterostructure.

An electrochemical impedance spectrum (EIS) has been obtained to investigate the impact of CoS_2 on the interfacial charge transfer kinetics. Fig. 4c depicts the Nyquist plots of $MgIn_2S_4$ and 20.5 wt% $CoS_2/MgIn_2S_4$ composite obtained at open circuit potential. A semi-arc is typically observed in EIS measurements when the electrode undergoes charge transfer [16]. The semiarc radius provides insight into the resistance to interfacial charge transfer, with the charge transfer resistance being proportional to the radius. Fig. 4c shows that the 20.5 wt% $CoS_2/MgIn_2S_4$ hybrids exhibit a smaller arc radius than $MgIn_2S_4$, suggesting a better charge transfer efficiency. The reduced resistivity is further confirmed by Hall effect tests (Fig. 4d), where the bare $MgIn_2S_4$ shows significantly higher resistivity than $CoS_2/MgIn_2S_4$. This can be attributed to the presence of CoS_2, which improves the conductance of $MgIn_2S_4$. Moreover, the Hall test demonstrates that the $CoS_2/MgIn_2S_4$ sample displays higher Hall mobility and charge carrier concentration than $MgIn_2S_4$. This indicates that the incorporation of CoS_2 and the presence of a strong IEF facilitate efficient separation and migration of photogenerated charges. Based on these results, it is obvious that the modification of $MgIn_2S_4$ with CoS_2 enhances the charge separation and transfer efficiency of the photocatalyst, significantly improving H_2 evolution.

DFT calculations provide further insight into the effective charge separation and transfer. The XRD results demonstrate a significant exposure of the CoS_2 (200) and $MgIn_2S_4$ (440) facets in the $CoS_2/MgIn_2S_4$ composites (Fig. 2a). Consequently, we conducted first-principles DFT simulations (Figs. 5a and 5b) targeting the cubic phases of CoS_2 (200) and $MgIn_2S_4$ (440) surfaces. The work functions of
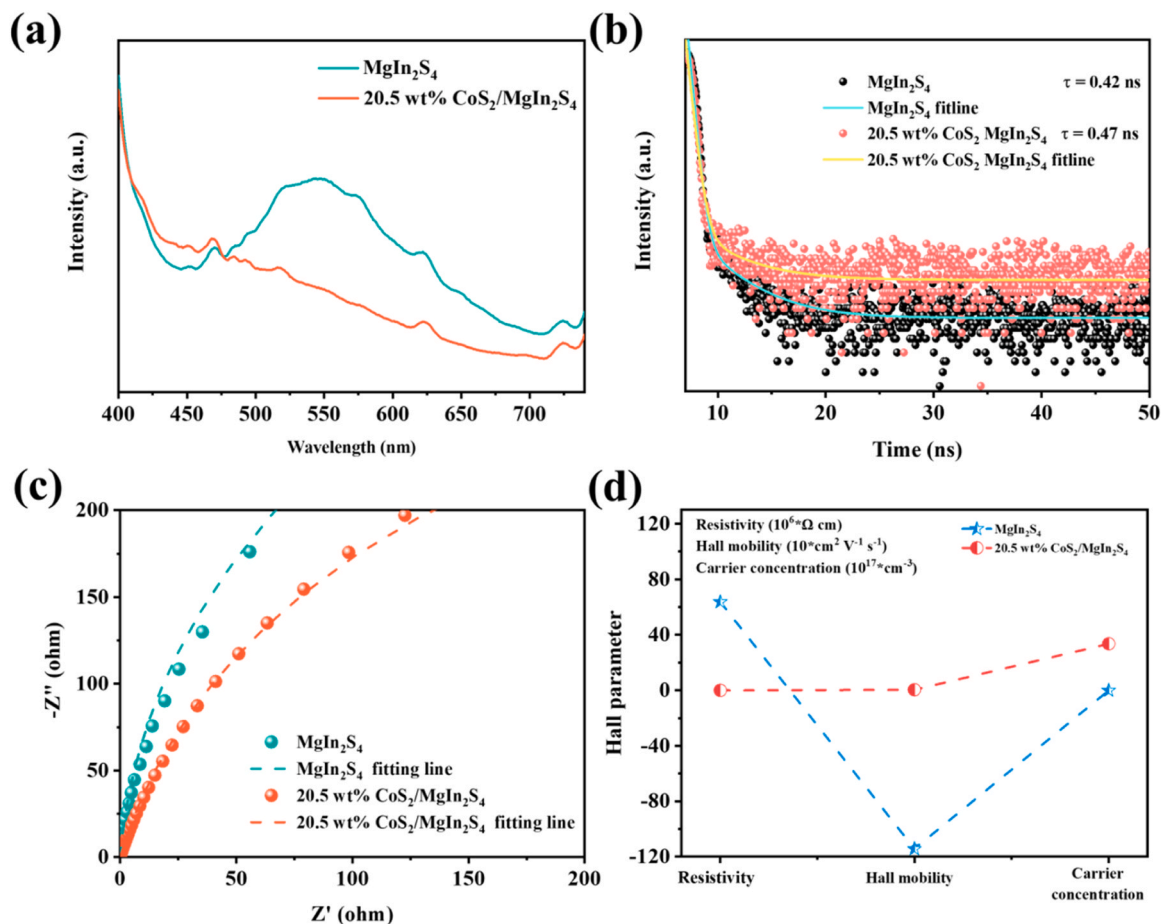
Fig. 4. (a) PL spectra and (b) time-resolved transient photoluminescence decay of $MgIn_2S_4$ and 20.5 wt% $CoS_2/MgIn_2S_4$ composite. (c) EIS plots and (d) Hall parameters of $MgIn_2S_4$ and 20.5 wt% $CoS_2/MgIn_2S_4$ composite.

CoS_2 and $MgIn_2S_4$ are 5.1 and 5.9 eV, respectively. The Fermi level (E_F) is then calculated with the equation: $E_F = -W_F + E_V$ [36], where W_F, and E_V denote the work function and vacuum energy (defined as 0 eV), respectively. The calculated Fermi energies of CoS_2 (200) and $MgIn_2S_4$ (440) are −5.1 eV and −5.9 eV, respectively. In this scenario, electrons tend to migrate from CoS_2 to $MgIn_2S_4$ upon contact, establishing a new Fermi level equilibrium. This electron migration induces a downward bending of the energy band in $MgIn_2S_4$, resulting in the formation of a space charge region where an Ohmic contact is established across the heterojunction. To further demonstrate charge transfer at the $CoS_2/MgIn_2S_4$ interface, the 3D charge-density and planar-averaged differential charge density have been calculated, as shown in Figs. 5c and 5d. The yellow and blue regions correspond to the accumulation and depletion of charges, respectively. This calculation reveals that the electrons are predominantly localized on the $MgIn_2S_4$ surface, while holes are concentrated near the CoS_2 side, indicating effective electron migration at the $CoS_2/MgIn_2S_4$ interface. This shift induces a strong interfacial electric field between the heterojunctions, proving a robust driving force to promote the photogenerated electron transfer from $MgIn_2S_4$ to CoS_2. Although DFT offers a powerful tool for the analysis of work functions and differential charge calculations, its accuracy is limited by inherent approximations in the exchange-correlation functional, surface and interface models, and charge distribution analysis methods. Recognizing these limitations is crucial for accurately interpreting DFT results. Therefore, our primary focus will shift to the experimental examination of the charge transfer process in the following section.

The experimental observation of photogenerated electron transfer in the $CoS_2/MgIn_2S_4$ composite has been confirmed by synchronous illumination X-ray photoelectron spectroscopy (SI-XPS), as shown in

Fig. 6a. Fig. S11 presents the full survey XPS spectra of 20.5 wt% $CoS_2/MgIn_2S_4$ measured in the dark and under irradiation, detecting Mg, In, S, and Co elements in the composite photocatalyst. In the dark, the Mg 1 s spectrum of pure $MgIn_2S_4$ exhibits a peak at approximately 1303.9 eV (Fig. 6b), attributed to Mg 1 s in a +2 oxidation state [14]. The In 3d spectra display two peaks at around 445.0 and 452.5 eV (Fig. 6c), corresponding to the $3d_{5/2}$ and $3d_{3/2}$ orbitals of In, respectively [16]. The S 2p spectra of pure $MgIn_2S_4$ (Fig. 6d) show two peaks at 161.9 eV (S $2p_{3/2}$) and 163.1 eV (S $2p_{1/2}$), indicative of the binding energy associated with S^{2-} [20]. In Fig. 6e, the high-resolution Co 2p XPS spectra of the 20.5 wt% $CoS_2/MgIn_2S_4$ composite reveal six distinct peaks. These peaks can be categorized into two sets of spin-orbit double peaks and two satellite peaks. The first set of double peaks is observed at 778.5 and 781.2 eV, while the second set is observed at 793.9 and 796.5 eV, corresponding to Co $2p_{3/2}$ and Co $2p_{1/2}$ binding energies, respectively. These peaks indicate that the composite catalyst contains both Co^{2+} and Co^{3+} species [36]. Generally, a change in the binding energy of an element is considered indicative of charge transfer between elements [49–51]. Compared with the XPS results obtained in the dark, the Co $2p_{1/2}$ and $2p_{3/2}$ signals of $CoS_2/MgIn_2S_4$ under illumination shift negatively by 0.3 eV and 0.5 eV, respectively, and the S $2p_{1/2}$ and $2p_{3/2}$ signals of $CoS_2/MgIn_2S_4$ under illumination shift negatively by 0.2 eV and 0.1 eV, while the Mg 1 s, and In $3d_{3/2}$ and $3d_{5/2}$ signals of $CoS_2/MgIn_2S_4$ peaks show a positive shift of 0.3, 0.1, and 0.1 eV (Fig. 6b-e), respectively. These results demonstrate that photogenerated electrons flow from $MgIn_2S_4$ to CoS_2 during light irradiation, which is in agreement with the results obtained by DFT calculations.

The photoelectron transfer dynamics can be further revealed through the analysis of surface photovoltage (SPV) spectra acquired from
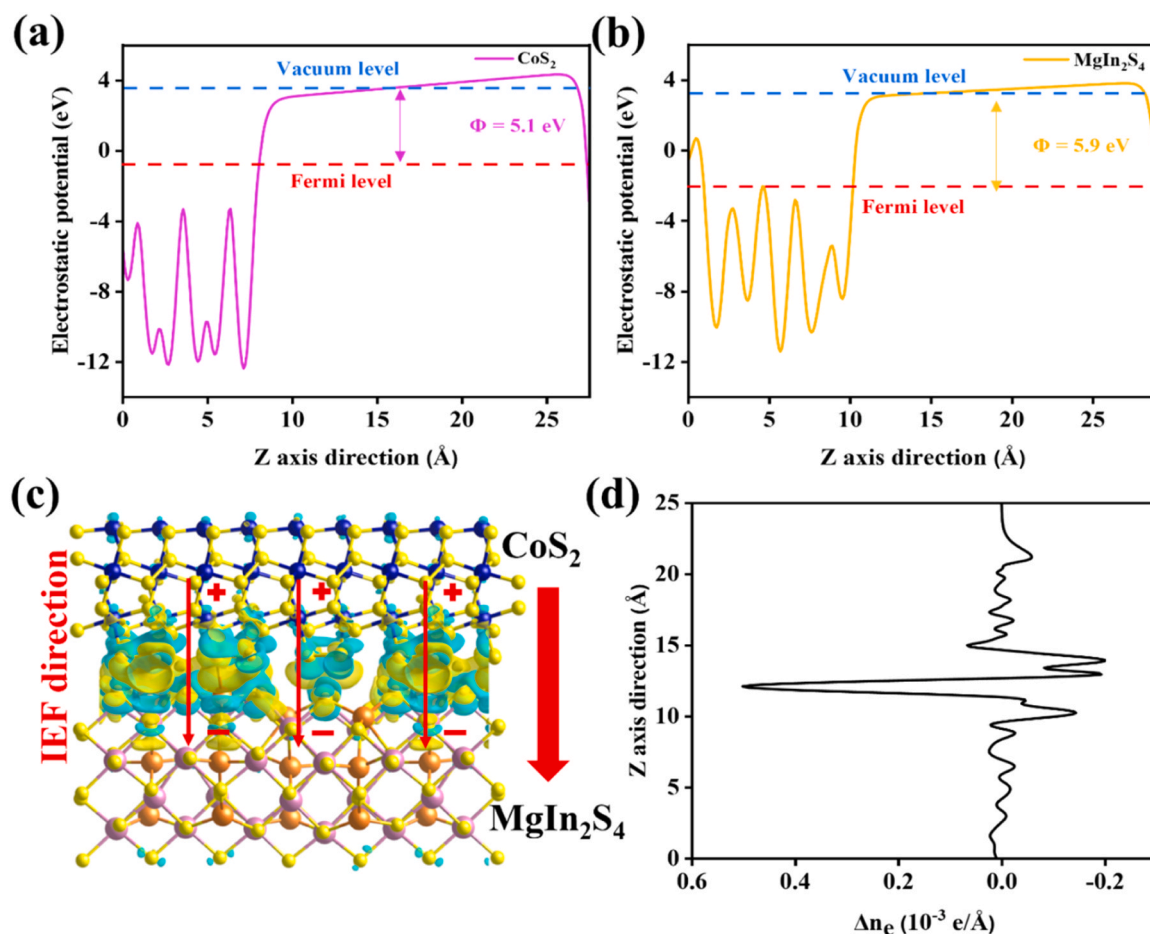
Fig. 5. (a-b) Work functions of CoS₂ and MgIn₂S₄. (c-d) 3D and planar averaged charge density difference for the 20.5 wt% CoS₂/MgIn₂S₄ model.

MgIn₂S₄ and 20.5 wt% CoS₂/MgIn₂S₄ samples (Fig. 6**f**). The MgIn₂S₄ sample exhibits a broad and positive SPV signal, aligning with its photoabsorption profile (Fig. 2**d**), particularly in the wavelength range of 300–600 nm. Interestingly, the introduction of CoS₂ results in a substantial reduction and near disappearance of the SPV signal. Typically, a higher SPV signal indicates enhanced charge separation efficiency, correlating with superior photocatalytic performance [52]. However, it is important to note that, despite demonstrating higher H₂ production activity, the CoS₂/MgIn₂S₄ sample displays a lower SPV response. This phenomenon is frequently observed in noble-metal-modified photocatalytic systems, where metals efficiently capture photogenerated electrons, decreasing surface charge and weakening SPV signals, while simultaneously improving photocatalytic activity [53]. Thus, similarly to noble metals, CoS₂ effectively captures photogenerated electrons of MgIn₂S₄, resulting in a reduced SPV signal. This electron transfer mechanism aligns with observations from *in situ* XPS, providing additional support for the existence of an Ohmic-junction.

The electron transfer dynamics at the CoS₂/MgIn₂S₄ interface can be further elucidated through irradiated KPFM. Fig. 7 presents the typical height image, contact potential difference (CPD) maps in both dark and light conditions, as well as the corresponding CPD curves of MgIn₂S₄ and 20.5 wt% CoS₂/MgIn₂S₄, using Xe lamps for sample irradiation. **Figs. 7d1** and **7d2** illustrate the CPD variation along a straight line for MgIn₂S₄ and CoS₂/MgIn₂S₄, before and after illumination. Prior illumination, MgIn₂S₄ exhibits a CPD distribution of −9.1–17.3 mV, increasing to −7.6–25.3 mV after illumination. The enhancement of CPD under illumination indicates the transfer of photogenerated electrons from MgIn₂S₄ to the catalyst surface [54]. In the dark, the CPD of CoS₂/MgIn₂S₄ ranges from 14.8 to 49.8 mV, and under light

illumination, it increases to 26.6–59.2 mV. Previous studies by Zhang et al. have established a positive correlation between the CPD of a particular material and its built-in electric field [55]. The CoS₂/MgIn₂S₄ heterojunction exhibits a higher CPD compared to the unmodified MgIn₂S₄ photocatalyst, indicating a more robust built-in electric field. This observation is consistent with the formation of an Ohmic junction. Furthermore, surface photovoltage can be determined by calculating the difference in contact potential difference (ΔCPD) under light and dark conditions (see Fig. S12 for details). It is evident that the ΔCPD of CoS₂/MgIn₂S₄ (20.7 mV) is significantly higher than the value of MgIn₂S₄ (16.1 mV), as shown in Figs. 7d1 and 7d2. These findings demonstrate a notable increase in the production of photogenerated carriers following light illumination for the CoS₂/MgIn₂S₄ system, aligning with the observed enhancement in the rate of hydrogen evolution. The increase in photogenerated carriers can be attributed to the efficient separation of charges at the interface of CoS₂/MgIn₂S₄, leading to a larger accumulation of electrons on the surface of CoS₂/MgIn₂S₄. Under the same illumination conditions, the higher electron accumulation at the CoS₂/MgIn₂S₄ surface is associated with the transfer of photogenerated electrons from MgIn₂S₄ to CoS₂, thereby increasing the number of electrons on the photocatalyst surface and substantially elevating the CPD. This increase in surface electron generation facilitates the reduction of water molecules to form H₂, ultimately enhancing the photocatalytic activity of MgIn₂S₄.

The application of DFT calculations to assess the hydrogen evolution reaction (HER) activity allows deeper insights into the role of CoS₂ in facilitating proton reduction on the MgIn₂S₄ photocatalyst surface. This is confirmed by the noteworthy correlation observed between the hydrogen-adsorption Gibbs free energy (ΔG_{H*}) and the HER activity
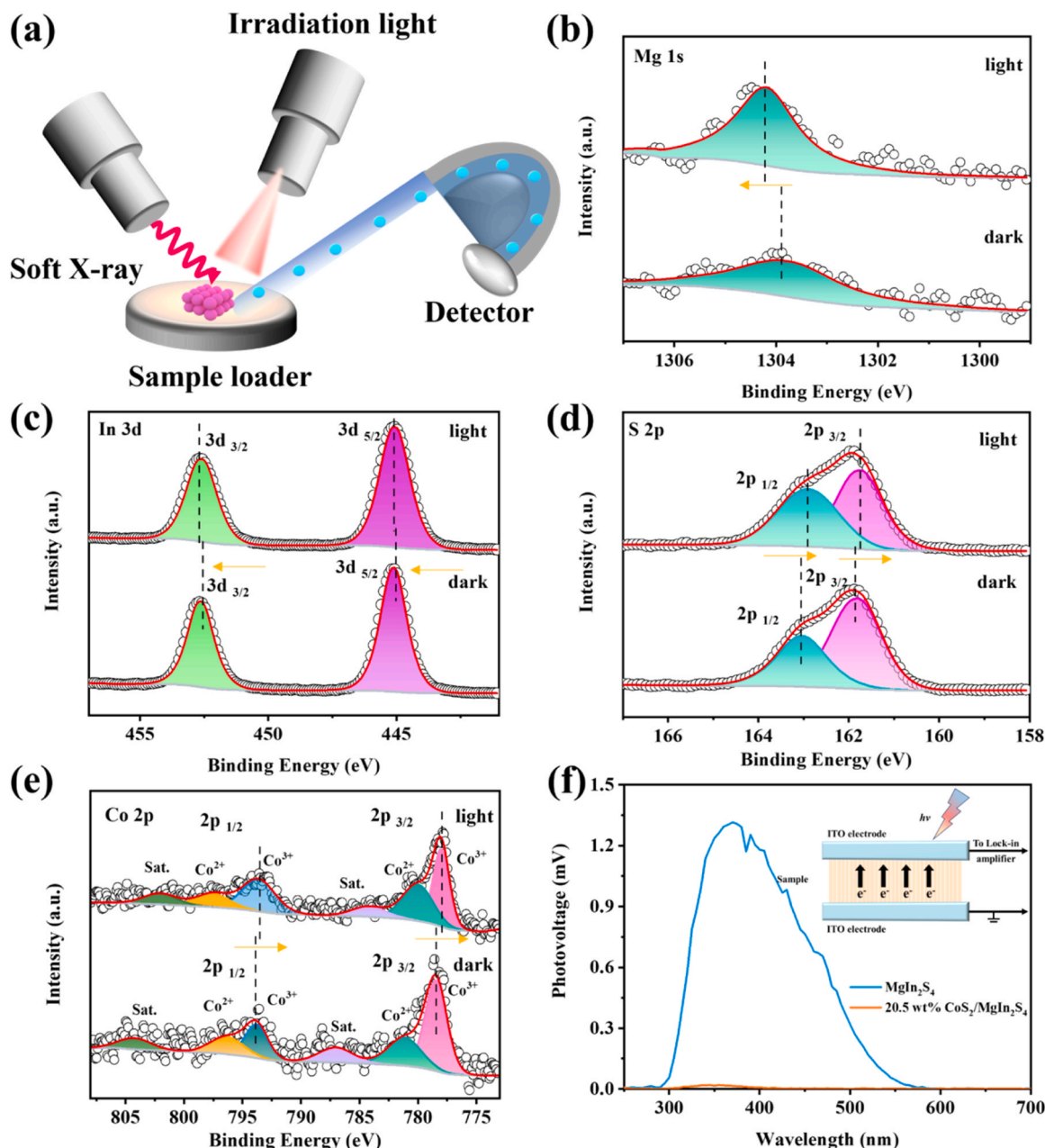
Fig. 6. (a) Schematic representation of the experimental setup for SI-XPS measurements. In-situ irradiated high-resolution XPS spectra of 20.5 wt% $CoS_2/MgIn_2S_4$ before and after light irradiation: (b) Mg 1 s, (c) In 3d, (d) S 2p and (e) Co 2p, and (f) SPV spectra of $MgIn_2S_4$ and 20.5 wt% $CoS_2/MgIn_2S_4$ samples.

[56]. Generally, a three-state diagram, involving an initial state of $H^+ + e^-$, an intermediate adsorbed H*, and a final product of H_2, is commonly used to summarize the entire HER process [57]. The ΔG_{H*} value, representing the Gibbs free energy of the intermediate state, is a critical determinant of the HER activity for various catalyst types [58]. According to the Sabatier principle, an excessively positive ΔG_{H*} value indicates weak H adsorption, while excessively negative values result in strong H* binding, hindering H_2 desorption [59]. Thus, for a HER catalyst to exhibit high efficiency, it is crucial that its ΔG_{H*} value approaches zero [60]. The predominant exposed facets of cubic CoS_2 and $MgIn_2S_4$ nanosheets are (200) and (440), as determined above (Fig. 3a). Consequently, DFT-based computations can be used to determine the ΔG_{H*} values for the sites located on the most exposed surface of CoS_2, $MgIn_2S_4$, and $CoS_2/MgIn_2S_4$. As depicted in Fig. 8a, the computed ΔG_{H*} values for CoS_2, $MgIn_2S_4$, and $CoS_2/MgIn_2S_4$ are 0.48, 1.58, and 0.44 eV, respectively. $CoS_2/MgIn_2S_4$ exhibits the lowest ΔG_{H*}, ensuring

efficient proton acceptance for H* formation and rapid hydrogen desorption. This aligns with its superior experimental HER performance, compared to CoS_2 and pure $MgIn_2S_4$. Consequently, $CoS_2/MgIn_2S_4$ demonstrates significantly stronger photocatalytic activity for H_2 evolution than $MgIn_2S_4$.

Moreover, the linear sweep voltammetry (LSV) measurements of the $CoS_2/MgIn_2S_4$ catalyst demonstrate superior HER catalytic activity compared to the $MgIn_2S_4$ catalyst alone. The LSV curves for $MgIn_2S_4$, and the 5 wt% $CoS_2/MgIn_2S_4$ samples are presented in Fig. 8b. A cathodic current onset potential of −0.34 V (vs. Ag/AgCl) is observed for $MgIn_2S_4$, indicating a substantial energy barrier for hydrogen reduction from water. In contrast, the 5 wt% $CoS_2/MgIn_2S_4$ exhibits a lower onset potential for the cathodic current, approximately −0.24 V (vs Ag/AgCl), and displays a much larger current density. These results confirm that CoS_2 is an effective electrocatalyst that promotes H_2 evolution, in agreement with previous studies [61,62]. Consequently, the
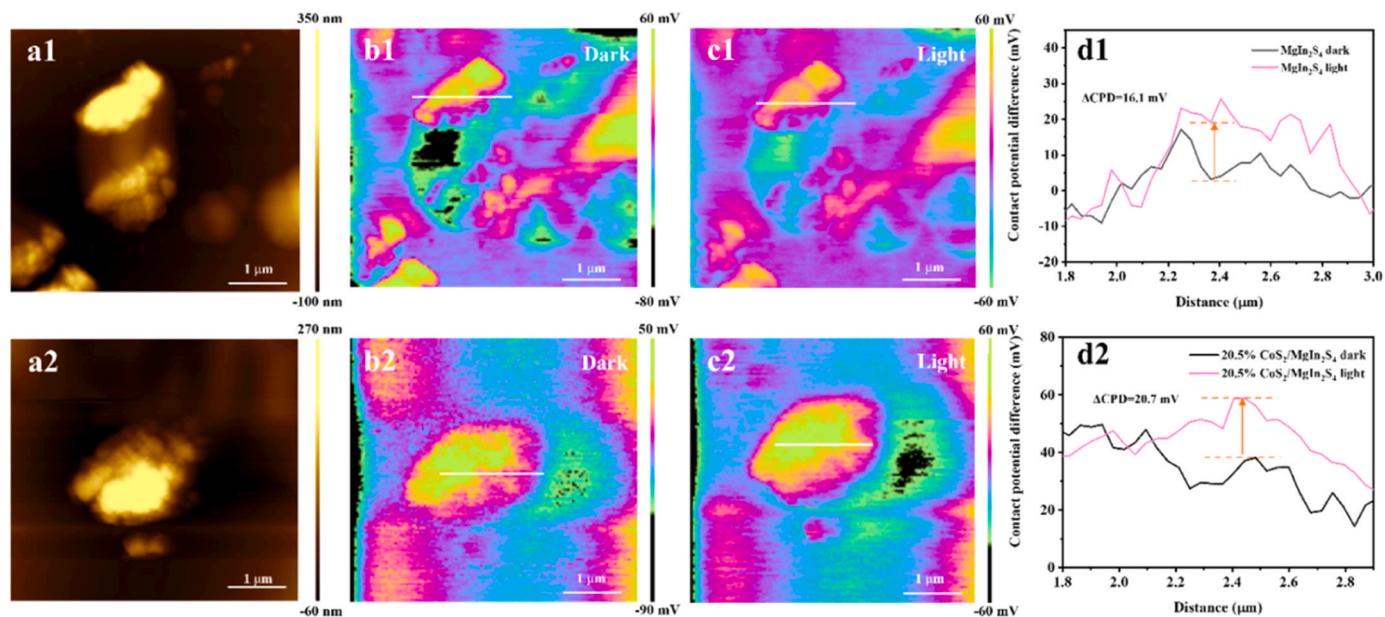
Fig. 7. (a) AFM image, (b-c) KPFM potential images and (d) corresponding contact potential difference curves along the line in the dark and under illumination for (a1–d1) MgIn$_2$S$_4$ and (a2–d2) 20.5 wt% CoS$_2$/MgIn$_2$S$_4$, respectively.
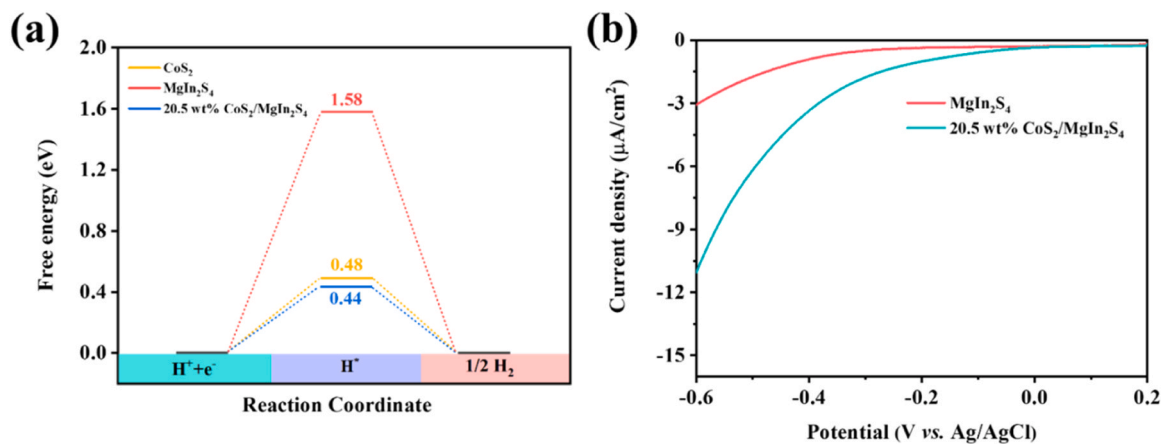

Fig. 8. (a) Gibbs free energy for H* adsorption on different catalysts of CoS$_2$, MgIn$_2$S$_4$ and 20.5 wt% CoS$_2$/MgIn$_2$S$_4$. (b) Current–voltage curves for proton reduction of MgIn$_2$S$_4$ and 20.5 wt% CoS$_2$/MgIn$_2$S$_4$, measured in the N$_2$-saturated Na$_2$SO$_4$ solution.
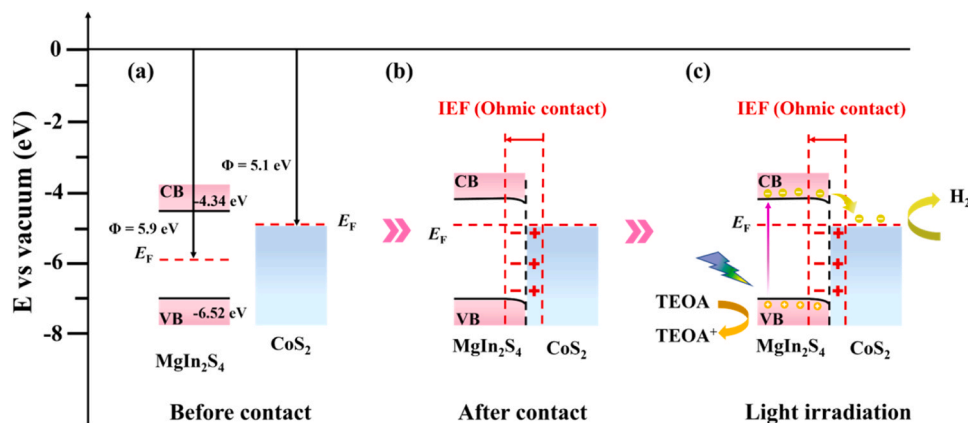
Fig. 9. Schematic illustration of IEF-induced CoS$_2$/MgIn$_2$S$_4$ Ohmic-Junction for H$_2$ production.

decoration of CoS_2 nanoparticles on $MgIn_2S_4$ nanosheets introduces new active sites, leading to a substantial enhancement in the intrinsic HER activity of the material.

A mechanistic insight into the photocatalytic H_2-evolution activity on the $CoS_2/MgIn_2S_4$ composites is summarized in Fig. 9. Firstly, the Mott-Schottky plot analysis (Fig. S13) has been employed to determine the energy band structure of $MgIn_2S_4$. The positive slope of the Mott-Schottky plot indicates that $MgIn_2S_4$ is a n-type semiconductor, and the measured flat-band potential (E_{fb}) is 0.04 V versus NHE. E_{fb} is generally 0.20 eV lower than the conduction band potential (E_{CB}) for n-type semiconductor [25]. As a result, the obtained E_{CB} of $MgIn_2S_4$ is -0.16 V vs. NHE. In the bare $MgIn_2S_4$ structure, the calculated band gap energy (E_g) is 2.18 eV, thus the valence band potential (E_{VB}) is 2.02 V vs NHE, determined through the formula $E_{VB} = E_{CB} + E_g$. Moreover, the energy levels of the band edges on the electrochemical scale (V vs. NHE) can be converted to the values E (eV) vs. vacuum energy level using the formula E (eV) $= -4.5 - E_{NHE}$ (V) [63]. Consequently, the E_{CB} and E_{VB} of $MgIn_2S_4$ are -4.34 and -6.52 eV vs. vacuum energy level, respectively. According to our DFT calculations, the Fermi level of CoS_2 (-5.1 eV) is higher than that of $MgIn_2S_4$ (-5.9 eV).

Based on the aforementioned results, Fig. 9a illustrates the band alignment between $MgIn_2S_4$ and CoS_2. Upon forming an intimate heterojunction, depicted in Fig. 9b, the free electrons in CoS_2 migrate to $MgIn_2S_4$, reducing the Fermi level (E_f) in CoS_2 and increasing the Fermi level of $MgIn_2S_4$ until equilibrium is reached. This electron transfer results in a positive charge on CoS_2 surface due to electron depletion and a negative charge on $MgIn_2S_4$ due to electron accumulation. The charge distribution establishes an IEF from CoS_2 to $MgIn_2S_4$, facilitating the separation and migration of photogenerated carriers. The accumulated electron induce a downward band bending in $MgIn_2S_4$, forming an Ohmic junction with CoS_2.

Upon light excitation, the photogenerated electrons in the $MgIn_2S_4$ conduction band accelerate towards the CoS_2 cocatalyst through the Ohmic junction. The absence of an interfacial barrier in the Ohmic contact allows the IEF to propel charge transfer, amplifying the separation and promoting the accumulation of electrons in CoS_2 for active participation in the hydrogen evolution reaction. The validity of the charge transfer mechanism is supported by the results obtained from *in situ* XPS spectra (Fig. 6a-e), SPV analysis (Fig. 6f), and *in situ* KPFM measurements (Fig. 7).

Furthermore, the superior catalytic activity of CoS_2 for H_2 evolution and its lower hydrogen-adsorption Gibbs free energy compared to $MgIn_2S_4$ (Fig. 8) result in rapid consumption of electrons on CoS_2 by adsorbed H^+ ions. The remaining holes on $MgIn_2S_4$ are oxidized by TEOA molecules, enhancing the photocatalytic efficiency of the $MgIn_2S_4$ photocatalyst for hydrogen production through the fulfillment of two primary functions: Enhancing charge carrier separation by capturing electrons from $MgIn_2S_4$ under light exposure, and acting as a catalyst for surface hydrogen reduction. Consequently, the $CoS_2/MgIn_2S_4$ material demonstrates superior photocatalytic hydrogen evolution performance and remarkable photostability.

4. Conclusions

In summary, this study successfully employed a facile hydrothermal method to incorporate CoS_2 nanoparticles onto the surface of 3D $MgIn_2S_4$ micro-flowers. The optimized $CoS_2/MgIn_2S_4$ composite, with a 20.5 wt% CoS_2 loading, demonstrated a remarkable hydrogen generation efficiency of 290 μmol g^{-1} h^{-1} and an AQE of 0.6% at 420 nm. These values were 3.1 times higher than those observed for pristine 3D $MgIn_2S_4$ micro-flowers. Notably, the CoS_2 loading minimally affected the crystal structure or morphology of $MgIn_2S_4$, yet contributed to an increase in specific surface area. This enhanced photocatalytic activity was attributed to the different work functions of CoS_2 and $MgIn_2S_4$, resulting in an Ohmic junction and a robust internal electric field at the $CoS_2/MgIn_2S_4$ interface. This facilitated an efficient transfer of

photogenerated electrons from $MgIn_2S_4$ to CoS_2. Furthermore, DFT calculations confirmed that the CoS_2 cocatalyst in $CoS_2/MgIn_2S_4$ possessed an optimal ΔG_{H*} value, beneficial to surface proton reduction at the catalyst/H_2O interface.

This study introduced an innovative approach to address the challenge of slow charge separation and transfer kinetics in the photocatalytic H_2 evolution process by incorporating a CoS_2 cocatalyst. The simultaneous enhancement of charge separation and transfer kinetics at the dual interfaces (semiconductor/cocatalyst and cocatalyst/H_2O), achieved through this strategy, significantly improved the H_2 evolution rate. Consequently, this research laid the foundation for the development of semiconductors-based photocatalysts with a multi-interface regulating strategy.

CRediT authorship contribution statement

Jiangshan Li: Writing – original draft, Investigation. **Jun Yao:** Writing – original draft, Investigation, Formal analysis. **Chenglin Wu:** Formal analysis. **Kangle Lv:** Writing – review & editing, Formal analysis, Conceptualization. **Qiang Yu:** Investigation, Formal analysis, Data curation. **Xiao Zhang:** Investigation, Formal analysis. **Sónia A.C. Carabineiro:** Writing – review & editing. **Xianqiang Xiong:** Writing – review & editing, Supervision, Resources, Formal analysis, Conceptualization.

Declaration of Competing Interest

The authors declare that they have no known competing financial interests or personal relationships that could have appeared to influence the work reported in this paper.

Data Availability

Data will be made available on request.

Acknowledgements

Appendix A. Supporting information

Supplementary data associated with this article can be found in the online version at doi:10.1016/j.apcatb.2024.123950.

References

[1] X. Feng, H. Shang, J. Zhou, X. Ma, X. Gao, D. Wang, B. Zhang, Y. Zhao, Heterostructured core–shell $CoS_{1.097}@ZnIn_2S_4$ nanosheets for enhanced photocatalytic hydrogen evolution under visible light, Chem. Eng. J. 457 (2023) 141192.

[2] M. Eisapour, H. Zhao, J. Zhao, T. Roostaei, Z. Li, A. Omidkar, J. Hu, Z. Chen, p-n heterojunction of nickel oxide on titanium dioxide nanosheets for hydrogen and value-added chemicals coproduction from glycerol photoreforming, J. Colloid Interface Sci. 647 (2023) 255–263.

[3] M. Yang, M. Li, Z. Jin, In situ XPS proved graphdiyne (C_nH_{2n-2})-based CoFe LDH/CuI/GD double S-scheme heterojunction photocatalyst for hydrogen evolution, Sep. Purif. Technol. 311 (2023) 123229.

[4] J. Li, M. Li, Y. Li, X. Guo, Z. Jin, Lotus-leaf-like $Bi_2O_2CO_3$ nanosheet combined with Mo_2S_3 for higher photocatalytic hydrogen evolution, Sep. Purif. Technol. 288 (2022) 120588.

[5] B. Wang, S. Guo, X. Xin, Y. Zhang, Y. Wang, C. Li, Y. Song, D. Deng, X. Li, A. J. Sobrido, M.-M. Titirici, Heat diffusion-induced gradient energy level in multishell bisulfides for highly efficient photocatalytic hydrogen production, Adv. Energy Mater. 10 (2020) 2001575.

[6] S. Guo, X. Li, X. Ren, L. Yang, J. Zhu, B. Wei, Optical and electrical enhancement of hydrogen evolution by $MoS_2@MoO_3$ core–shell nanowires with designed tunable plasmon resonance, Adv. Funct. Mater. 28 (2018) 1802567.

[7] J. Ran, G. Gao, F.-T. Li, T.-Y. Ma, A. Du, S.-Z. Qiao, Ti_3C_2 MXene co-catalyst on metal sulfide photo-absorbers for enhanced visible-light photocatalytic hydrogen production, Nat. Commun. 8 (2017) 13907.

[8] Y. Chao, P. Zhou, N. Li, J. Lai, Y. Yang, Y. Zhang, Y. Tang, W. Yang, Y. Du, D. Su, Y. Tan, S. Guo, Ultrathin visible-light-driven Mo incorporating In_2O_3–$ZnIn_2Se_4$ Z-scheme nanosheet photocatalysts, Adv. Mater. 31 (2019) 1807226.

[9] Z.-K. Shen, M. Cheng, Y.-J. Yuan, L. Pei, J. Zhong, J. Guan, X. Li, Z.-J. Li, L. Bao, X. Zhang, Z.-T. Yu, Z. Zou, Identifying the role of interface chemical bonds in activating charge transfer for enhanced photocatalytic nitrogen fixation of Ni_2P-black phosphorus photocatalysts, Appl. Catal. B 295 (2021) 120274.

[10] P. Ganguly, M. Harb, Z. Cao, L. Cavallo, A. Breen, S. Dervin, D.D. Dionysiou, S. C. Pillai, 2D nanomaterials for photocatalytic hydrogen production, ACS Energy Lett. 4 (2019) 1687–1709.

[11] Y.-J. Yuan, N. Lu, L. Bao, R. Tang, F.-G. Zhang, J. Guan, H.-D. Wang, Q.-Y. Liu, Q. Cheng, Z.-T. Yu, Z. Zou, SiP Nanosheets: A metal-free two-dimensional photocatalyst for visible-light photocatalytic H_2 production and nitrogen fixation, ACS Nano 16 (2022) 12174–12184.

[12] H. Jin, C. Guo, X. Liu, J. Liu, A. Vasileff, Y. Jiao, Y. Zheng, S.-Z. Qiao, Emerging two-dimensional nanomaterials for electrocatalysis, Chem. Rev. 118 (2018) 6337–6408.

[13] Y. Wang, X. Fang, J. Zeng, S. Li, X. Wang, B. Zhang, 0D/2D/3D ternary $Au/Ti_3C_2/TiO_2$ photocatalyst based on accelerating charge transfer and enhanced stability for efficiently hydrogen production, Appl. Surf. Sci. 615 (2023) 156397.

[14] K. Qi, M. Song, X. Xie, Y. Wen, Z. Wang, B. Wei, Z. Wang, CQDs/biochar from reed straw modified Z-scheme $MgIn_2S_4/BiOCl$ with enhanced visible-light photocatalytic performance for carbamazepine degradation in water, Chemosphere 287 (2022) 132192.

[15] G. Swain, S. Sultana, K. Parida, Constructing a novel surfactant-free MoS_2 nanosheet modified $MgIn_2S_4$ marigold microflower: an efficient visible-light driven ^2D–^2D p-n heterojunction photocatalyst toward HER and pH regulated NRR, ACS Sustain. Chem. Eng. 8 (2020) 4848–4862.

[16] H.-Y. Liu, C.-G. Niu, H. Guo, C. Liang, D.-W. Huang, L. Zhang, Y.-Y. Yang, L. Li, In suit constructing 2D/1D $MgIn_2S_4/CdS$ heterojunction system with enhanced photocatalytic activity towards treatment of wastewater and H_2 production, J. Colloid Interface Sci. 576 (2020) 264–279.

[17] C. Zeng, Q. Zeng, C. Dai, L. Zhang, Y. Hu, Fabrication of Bi-$BiOCl/MgIn_2S_4$ heterostructure with step-scheme mechanism for carbon dioxide photoreduction into methane, J. CO2 Util. 45 (2021) 101453.

[18] L. Jing, Y. Xu, M. Xie, J. Liu, J. Deng, L. Huang, H. Xu, H. Li, Three dimensional polyaniline/$MgIn_2S_4$ nanoflower photocatalysts accelerated interfacial charge transfer for the photoreduction of Cr(VI), photodegradation of organic pollution and photocatalytic H_2 production, Chem. Eng. J. 360 (2019) 1601–1612.

[19] Z.-w Zhang, R.-t Guo, J.-y Tang, Y.-f Miao, J.-w Gu, W.-g Pan, Fabrication of Bi-$BiOCl/MgIn_2S_4$ heterostructure with step-scheme mechanism for carbon dioxide photoreduction into methane, J. CO2 Util. 45 (2021) 101453.

[20] L. Acharya, G. Swain, B.P. Mishra, R. Acharya, K. Parida, Development of $MgIn_2S_4$ microflower-embedded exfoliated B-doped g-C_3N_4 nanosheets: p–n heterojunction photocatalysts toward photocatalytic water reduction and H_2O_2 production under visible-light irradiation, ACS Appl. Energy Mater. 5 (2022) 2838–2852.

[21] W. Yang, Y. Dong, Z. Wang, Y. Li, C. Dai, D. Ma, Y. Jia, Z. Yang, C. Zeng, Synthesis, characterization, and photocatalytic activity of stannum-doped $MgIn_2S_4$, Micro, J. Alloy. Compd. 860 (2021) 158446.

[22] S.P. Tripathy, S. Subudhi, A. Ray, P. Behera, G. Swain, M. Chakraborty, K. Parida, $MgIn_2S_4/UiO-66-NH_2$ MOF-based heterostructure: visible-light-responsive Z-scheme-mediated synergistically enhanced photocatalytic performance toward hydrogen and oxygen evolution, Langmuir 39 (2023) 7294–7306.

[23] L. Biswal, L. Acharya, B.P. Mishra, S. Das, G. Swain, K. Parida, Interfacial solid-state mediator-based Z-scheme heterojunction $TiO_2@Ti_3C_2/MgIn_2S_4$ microflower for efficient photocatalytic pharmaceutical micropollutant degradation and hydrogen generation: stability, kinetics, and mechanistic insights, ACS Appl. Energy Mater. 6 (2023) 2081–2096.

[24] W. Yang, S.-S. Xu, Y. Niu, Y. Zhang, J. Xu, $Ni_{12}P_5$-supported marigold-shaped $CdIn_2S_4$: a 2D/3D non-noble-metal catalyst for visible-light-driven hydrogen production, J. Phys. Chem. C 127 (2023) 4853–4861.

[25] K. Chen, Y. Shi, P. Shu, Z. Luo, W. Shi, F. Guo, Construction of core–shell $FeS_2@ZnIn_2S_4$ hollow hierarchical structure S-scheme heterojunction for boosted photothermal-assisted photocatalytic H_2 production, Chem. Eng. J. 454 (2023) 140053.

[26] G.Z.S. Ling, S.-F. Ng, W.-J. Ong, Tailor-engineered 2D cocatalysts: harnessing electron–hole redox center of 2D g-C_3N_4 photocatalysts toward solar-to-chemical conversion and environmental purification, Adv. Funct. Mater. 32 (2022) 2111875.

[27] H. Zhao, L. Jian, M. Gong, M. Jing, H. Li, Q. Mao, T. Lu, Y. Guo, R. Ji, W. Chi, Y. Dong, Y. Zhu, Transition-metal-based cocatalysts for photocatalytic water splitting, Small Struct. 3 (2022) 2100229.

[28] Z. Liang, R. Shen, Y.H. Ng, P. Zhang, Q. Xiang, X. Li, A review on 2D MoS_2 cocatalysts in photocatalytic H_2 production, J. Mater. Sci. Technol. 56 (2020) 89–121.

[29] K. Li, S. Zhang, Y. Li, J. Fan, K. Lv, MXenes as noble-metal-alternative co-catalysts in photocatalysis, Chin. J. Catal. 42 (2021) 3–14.

[30] R.-T. Guo, Z.-R. Zhang, C. Xia, C.-F. Li, W.-G. Pan, Recent progress of cocatalysts loaded on carbon nitride for selective photoreduction of CO_2 to CH_4, Nanoscale 15 (2023) 8548–8577.

[31] W. Tan, Y. Li, W. Jiang, C. Gao, C. Zhuang, CdS nanospheres decorated with NiS quantum dots as nobel-metal-free photocatalysts for efficient hydrogen evolution, ACS Appl. Energy Mater. 3 (2020) 8048–8054.

[32] X. Cai, Z. Zeng, Y. Liu, Z. Li, X. Gu, Y. Zhao, L. Mao, J. Zhang, Visible-light-driven water splitting by yolk-shelled $ZnIn_2S_4$-based heterostructure without noble-metal co-catalyst and sacrificial agent, Appl. Catal. B 297 (2021) 120391.

[33] S. Wang, B.Y. Guan, X. Wang, X.W.D. Lou, Formation of hierarchical $Co_9S_8@ZnIn_2S_4$ heterostructured cages as an efficient photocatalyst for hydrogen evolution, J. Am. Chem. Soc. 140 (2018) 15145–15148.

[34] J. Sun, S. Yang, Z. Liang, X. Liu, P. Qiu, H. Cui, J. Tian, Two-dimensional/one-dimensional molybdenum sulfide (MoS_2) nanoflake/graphitic carbon nitride (g-C_3N_4) hollow nanotube photocatalyst for enhanced photocatalytic hydrogen production activity, J. Colloid Interface Sci. 567 (2020) 300–307.

[35] S. Yang, X. Guo, K. Liu, Y. Li, T. Li, X. Gu, R. Arenal, X. Zheng, W. Li, C. Sun, H. Huang, F. Huang, Size effect of CoS_2 cocatalyst on photocatalytic hydrogen evolution performance of g-C_3N_4, J. Colloid Interface Sci. 635 (2023) 305–315.

[36] J. Tang, B. Gao, J. Pan, L. Chen, Z. Zhao, S. Shen, J.-K. Guo, C.-T. Au, S.-F. Yin, CdS nanorods anchored with CoS_2 nanoparticles for enhanced photocatalytic hydrogen production, Appl. Catal. A 588 (2019) 117281.

[37] X. Chen, Y. Yu, J. Li, P. Deng, C. Wang, Y. Hua, Y. Shen, X. Tian, Recent advances in cobalt disulfide for electrochemical hydrogen evolution reaction, Int. J. Hydrogen Energy 48 (2023) 9231–9243.

[38] H. Li, P. Deng, Y. Hou, Cobalt disulfide/graphitic carbon nitride as an efficient photocatalyst for hydrogen evolution reaction under visible light irradiation, Mater. Lett. 229 (2018) 217–220.

[39] X. Xi, Q. Dang, G. Wang, W. Chen, L. Tang, ZIF-67-derived flower-like $ZnIn_2S_4@CoS_2$ heterostructures for photocatalytic hydrogen production, N. J. Chem. 45 (2021) 20289–20295.

[40] B.Q. Qiu, C.X. Li, X.Q. Shen, W.L. Wang, H. Ren, Y. Li, J. Tang, Revealing the size effect of metallic CoS_2 on CdS nanorods for photocatalytic hydrogen evolution based on Schottky junction, Appl. Catal. A 592 (2020) 117377.

[41] L. Li, J. Xu, J. Ma, Z. Liu, Y. Li, A bimetallic sulfide $CuCo_2S_4$ with good synergistic effect was constructed to drive high performance photocatalytic hydrogen evolution, J. Colloid Interface Sci. 552 (2019) 17–26.

[42] H. Yin, T. Fan, Y. Cao, P. Li, X. Yao, X. Liu, Construction of three-dimensional $MgIn_2S_4$ nanoflowers/two-dimensional oxygen-doped g-C_3N_4 nanosheets direct Z-scheme heterojunctions for efficient Cr(VI) reduction: insight into the role of superoxide radicals, J. Hazard. Mater. 420 (2021) 126567.

[43] T. Liu, Y. Xiong, X. Wang, Y. Xue, W. Liu, J. Tian, Dual cocatalysts and vacancy strategies for enhancing photocatalytic hydrogen production activity of $Zn_3In_2S_6$ nanosheets with an apparent quantum efficiency of 66.20, J. Colloid Interface Sci. 640 (2023) 31–40.

[44] S. Zhang, S. Du, Y. Wang, Z. Han, X. Li, G. Li, Q. Hu, H. Xu, C. He, P. Fang, Synergy of yolk-shelled structure and tunable oxygen defect over $CdS/CdCO_3$-CoS_2: wide band-gap semiconductors assist in efficient visible-light-driven H_2 production and CO_2 reduction, Chem. Eng. J. 454 (2023) 140113.

[45] Y. Cai, Y. Shi, W. Shi, S. Bai, S. Yang, F. Guo, A one-photon excitation pathway in 0D/3D $CoS_2/ZnIn_2S_4$ composite with nanoparticles on micro-flowers structure for boosted visible-light-driven photocatalytic hydrogen evolution, Compos. Part B Eng. 238 (2022) 109955.

[46] N. Denisov, J. Yoo, P. Schmuki, Effect of different hole scavengers on the photoelectrochemical properties and photocatalytic hydrogen evolution performance of pristine and Pt-decorated TiO_2 nanotubes, Electrochim. Acta 319 (2019) 61–71.

[47] S. Meng, S. Chen, X. Gu, H. Wu, Q. Meng, J. Zhang, S. Chen, X. Fu, D. Liu, W. Lei, Efficient photocatalytic H_2 evolution, CO_2 reduction and N_2 fixation coupled with organic synthesis by cocatalyst and vacancies engineering, Appl. Catal. B 285 (2021) 119789.

[48] M. Zhao, S. Liu, S. Chen, S. Zhang, S.A.C. Carabineiro, K. Lv, A novel S-scheme 3D $ZnIn_2S_4/WO_3$ heterostructure for improved hydrogen production under visible light irradiation, Chin. J. Catal. 43 (2022) 2615–2624.

[49] P. Zhang, Y. Li, Y. Zhang, R. Hou, X. Zhang, C. Xue, S. Wang, B. Zhu, N. Li, G. Shao, Photogenerated electron transfer process in heterojunctions: in situ irradiation XPS, Small Methods 4 (2020) 2000214.

[50] Y. Wang, M. Liu, F. Fan, G. Li, J. Duan, Y. Li, G. Jiang, W. Yao, Enhanced full-spectrum photocatalytic activity of 3D carbon-coated C_3N_4 nanowires via giant interfacial electric field, Appl. Catal. B 318 (2022) 121829.

[51] Y. Li, L. Wang, F. Zhang, W. Zhang, G. Shao, P. Zhang, Detecting and quantifying wavelength-dependent electrons transfer in heterostructure catalyst via in situ irradiation XPS, Adv. Sci. 10 (2023) 2205020.

[52] J. Li, Q. Yu, X. Zhang, X. Xiong, Y. Jin, D. Han, B. Yu, J. Yao, G. Dai, Coupling CoS_2 and $CaIn_2S_4$ for efficient electron trapping and improved surface catalysis to promote solar hydrogen evolution, Int. J. Hydrogen Energy 52 (2023) 314–326.

[53] S.W. Verbruggen, J.J.J. Dirckx, J.A. Martens, S. Lenaerts, Surface photovoltage measurements: a quick assessment of the photocatalytic activity? Catal. Today 209 (2013) 215–220.

[54] R. Zhang, H. Wang, Y. Li, D. Wang, Y. Lin, Z. Li, T. Xie, Investigation on the photocatalytic hydrogen evolution properties of Z-scheme Au NPs/CuInS$_2$/NCN-CN$_x$ composite photocatalysts, ACS Sustain. Chem. Eng. 9 (2021) 7286–7297.

[55] J. Li, L. Cai, J. Shang, Y. Yu, L. Zhang, Giant enhancement of internal electric field boosting bulk charge separation for photocatalysis, Adv. Mater. 28 (2016) 4059–4064.

[56] S.S. Gupta, M.A. van Huis, Intermetallic differences at CdS–metal (Ni, Pd, Pt, and Au) interfaces: from single-atom to subnanometer metal clusters, J. Phys. Chem. C 123 (2019) 9298–9310.

[57] H. Zhang, Y. Dong, S. Zhao, G. Wang, P. Jiang, J. Zhong, Y. Zhu, Photochemical preparation of atomically dispersed nickel on cadmium sulfide for superior photocatalytic hydrogen evolution, Appl. Catal. B 261 (2020) 118233.

[58] J. Zhu, Q. Bi, Y. Tao, W. Guo, J. Fan, Y. Min, G. Li, Mo-modified ZnIn$_2$S$_4$@NiTiO$_3$ S-scheme heterojunction with enhanced interfacial electric field for efficient visible-light-driven hydrogen evolution, Adv. Funct. Mater. 33 (2023) 2213131.

[59] X. Lu, A. Tong, D. Luo, F. Jiang, J. Wei, Y. Huang, Z. Jiang, Z. Lu, Y. Ni, Confining single Pt atoms from Pt clusters on multi-armed CdS for enhanced photocatalytic hydrogen evolution, J. Mater. Chem. A 10 (2022) 4594–4600.

[60] Y. Zheng, Y. Jiao, M. Jaroniec, S.Z. Qiao, Advancing the electrochemistry of the hydrogen-evolution reaction through combining experiment and theory, Angew. Chem. Int. Ed. 54 (2015) 52–65.

[61] M. Wang, W. Zhang, F. Zhang, Z. Zhang, B. Tang, J. Li, X. Wang, Theoretical expectation and experimental implementation of in situ Al-doped CoS$_2$ nanowires on dealloying-derived nanoporous intermetallic substrate as an efficient electrocatalyst for boosting hydrogen production, ACS Catal. 9 (2019) 1489–1502.

[62] Y. Hu, Y. Qi, M. Pi, Y. Qiao, L. Hao, Y. Wang, H. Guan, J. Feng, Nanostructure and stoichiometry tailoring of CoS$_2$ for high performance hydrogen evolution reaction, Int. J. Hydrogen Energy 48 (2023) 16279–16285.

[63] P. Dong, C. Meng, Y. Yan, B. Zhang, W. Wang, X. Xi, J. Zhang, Ag–Pt bimetallic composite supported on defective C$_3$N$_x$ nanosheets for plasmon hot electron-mediated photocatalytic H$_2$ evolution, Int. J. Hydrogen Energy 48 (2023) 18670–18684.